

A Physics-based Virtual Reality Simulation Framework for Neonatal Endotracheal Intubation

Xiao Xiao¹ Shang Zhao¹ Yan Meng¹ Lamia Soghier² Xiaoke Zhang¹ James Hahn¹

¹George Washington University*

²National Children's Health Systems[†]

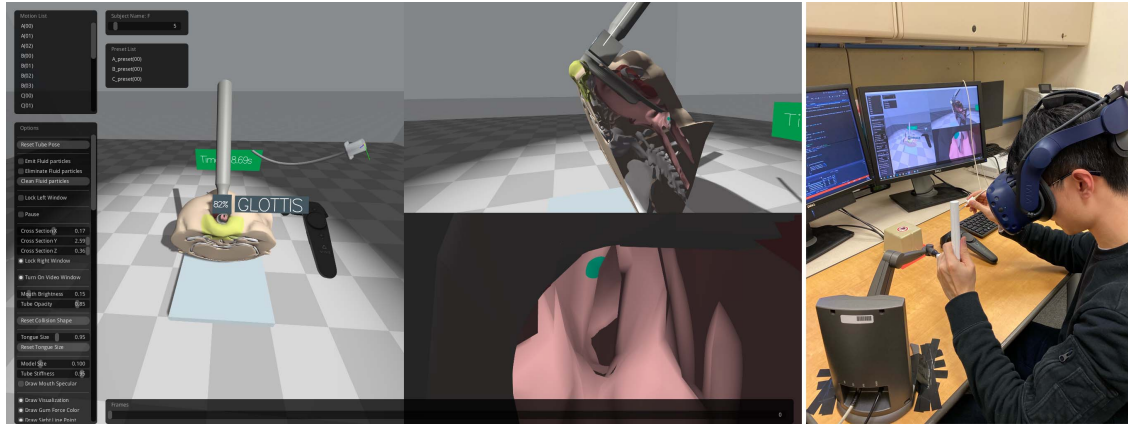


Figure 1: (left) Screenshot of the simulation with left-eye view from the HMD, cross-sectional view and video laryngoscopic view. Enhanced visualization tools are shown to give real-time visual feedback; (right) a user interacting with the simulator through the HMD with a haptic device and an EM sensor.

ABSTRACT

Neonatal endotracheal intubation (ETI) is a complex procedure. Low intubation success rates for pediatric residents indicate the current training regimen is inadequate for achieving positive patient outcomes. Computer-based training systems in this field have been limited due to the complex nature of simulating in real-time, the anatomical structures, soft tissue deformations and frequent tool interactions with large forces which occur during actual patient intubation. This paper addresses the issues of neonatal ETI training in an attempt to bridge the gap left by traditional training methods. We propose a fully interactive physics-based virtual reality (VR) simulation framework for neonatal ETI that converts the training of this medical procedure to a completely immersive virtual environment where both visual and physical realism were achieved. Our system embeds independent dynamics models and interaction devices in separate modules while allowing them to interact with each other within the same environment, which offers a flexible solution for multi-modal medical simulation scenarios. The virtual model was extracted from CT scans of a neonatal patient, which provides realistic anatomical structures and was parameterized to allow variations in a range of features that affect the level of difficulty. Moreover, with this manikin-free VR system, we can capture and visualize an even larger set of performance parameters in relation to the internal geometric change of the virtual model for real-time guidance and post-trial assessment. Lastly, validation study results from a group of neonatologists are presented demonstrating that VR is a promising platform to train medical professionals effectively for this procedure.

*e-mail: xxfall2012@gwu.edu, edwinz@gwu.edu, mengy@gwu.edu, xkzhang@gwu.edu, hahn@gwu.edu

[†]e-mail: lsoghier@childrensnational.org

Index Terms: Computing methodologies—Computer graphics—Graphics systems and interfaces—Virtual reality; Computing methodologies—Computer graphics—Animation—Physical simulation; Computing methodologies—Modeling and simulation—Simulation types and techniques—Real-time simulation; Human-centered computing—Human computer interaction (HCI)—Interaction devices—Haptic devices

1 INTRODUCTION

Neonatal ETI is a time-sensitive resuscitation procedure essential for ventilation of newborns. It requires an unusually high level of skill due to the narrow airways, relatively large tongue, anterior glottic position and low respiratory reserve of neonates [3]. Given the difficulty of the procedure and the high rate of complications in this population, effective training is crucial for achieving positive patient outcomes [9] [10] [31]. The best way to master the ETI skills is to perform as many supervised practice trials as possible on patients. However, pediatric residents experience an average of 3 clinical opportunities to perform ETI during 3 years of residency [6], a number that falls far short of the 47-57 intubations required for a consistent 90% success rate [13]. Due to this limitation, ETI training is heavily reliant on physical manikins, which allow learners to achieve some level of competence prior to clinical exposure. However, practicing on current commercial airway manikins has not been found to be a substitute for training on patients [15] [24] [33] [35]. Most of the manikins and simulator-based training typically provide little variation in anatomy or difficulty level and do not realistically model the look, feel and motions inherent in real patients. Consequently, learners who train on one manikin with a single airway model may develop model-specific techniques that may not transfer to patients or even other manikins [27]. Moreover, the small size of the intubation space in neonatal models prevent learners from observing the events occurring within the manikin or the patient; learners have poor knowledge about what went wrong and how to

improve. Lastly, assessment of ETI performance under artificially ideal conditions likely overestimate trainees' skill level since they do not mimic the stressors and distractions that are inherent in the real clinical environment. Thus, there is a pressing need for innovative training modalities that can bridge the gap left by traditional training and thereby allow rapid skill acquisition.

VR-based training systems offer an elegant solution to the current need for better training in the medical field, since realistic and configurable training environments can be created without any restriction for repetitive practicing. Many VR simulators have been deployed for training medical professionals; however, due to the various unsolved technical issues, ETI simulation has not been widely used. Such issues include modelling complex anatomical structures and large soft tissue deformations, handling collisions of frequent tool interactions with large forces and rendering realistic haptic feedback.

In this paper, we aim to address the notable gaps in previous work by developing a practical and efficient framework for training-oriented ETI simulation. The contributions of this study are:

- Build a fully interactive VR simulation system that integrates, in the same environment, different dynamics models and interaction devices, which provides both visual and physical realism;
- Create realistic anatomical virtual models from CT scans of neonatal patients that can parametrically adjust features that vary the levels of difficulty;
- Simulate physics of the virtual models, including bones, soft tissues and fluids in a unified representation based on position-based dynamics (PBD);
- Capture and visualize a large set of performance parameters during the entire procedure for real-time guidance and post-trial assessment;
- Evaluate the realism of the VR simulator by conducting a validation study with a group of neonatologists.

2 RELATED WORK

2.1 Simulators

ETI simulation is often associated with physical manikin simulators rather than computer-based simulators. A few VR ETI simulation systems have been developed; however, most of them allow limited interactions and/or do not simulate the physics of the virtual models. Mayrose et al. [18] [19] developed an intubation simulator that uses force-based mass-spring model for soft tissue deformation. In order to achieve real-time performance, the system only allows the interactions of the laryngoscope blade and the endotracheal tube (ETT) with relevant soft tissues of the virtual model, which is not fully interactive. The laryngoscope and the ETT are manipulated through a single haptic device, which does not allow bimanual operation. The graphics are projected through a semi-transparent mirror to allow the user to view through 3D glasses, which does not provide a fully immersive experience in a virtual environment. Demirel et al. [7] developed a virtual airway skills trainer in which only two tasks prior to the ETI procedure were simulated. Although their system provides an immersive experience with VR devices, it does not include simulation of the actual intubation. Rajeswaran et al. [29] developed a VR-based immersive trainer that allows the user to carry out intubation by following step-by-step on-screen instructions. However, their virtual model only allows limited interactions, such as head elevation and jaw opening. Neither collision detection of the tools with the virtual model nor soft tissue deformation was implemented, both of which are essential for realistic simulation. The laryngoscope and the ETT are controlled by two hand controllers, which is not intuitive and does not allow force feedback.

All of these simulation systems are not capable of simulating the entire ETI procedure because of the aforementioned unsolved issues. In contrast, our physics-based VR simulator provides a complete picture of simulating the entire ETI procedure and allows the user to

fully interact with the virtual models and bimanually manipulate the medical instruments in real time.

2.2 Deformation Models

The simulation of deformable objects has been an active research topic in computer graphics over the past decades. Traditional force-based dynamics, including finite element methods, mass-spring systems, meshless methods and particle systems, have been widely used [2] [23]. These approaches model deformable objects through the manipulation of internal and external forces, which are transformed into accelerations, using Newton's second law of motion. The positions of elements that comprise an object are then determined through numerical integration of the derived accelerations, which usually cause overshooting under large time steps. These force-based approaches can provide an accurate computation model for elastic objects of different material properties but require high computational cost. Therefore, simulating the entire medical procedure at interactive rates using force-based methods is not practical.

PBD [21] has gained great popularity recently due to its simplicity, high efficiency, unconditional stability and real-time performance. In contrast to force-based methods that achieve equilibrium configurations through the integration of accelerations, PBD approach directly projects positions as a solution to a set of geometrical constraints, which eliminates the overshooting problem in force-based methods and simplifies the implementation process. Although PBD is not as accurate as force-based methods, its efficiency and controllability far outperform those methods in simulating medical procedures while providing visually plausible results [5]. The PBD approach has already been successfully applied in the medical field, such as surgical thread simulation [14], laparoscopic surgery simulation [28], surgical cutting [4] and robotic surgery simulation [11]. Various haptic devices were integrated to allow the user to manipulate virtual tools in these simulators. However, unlike these procedures where small forces are involved, ETI procedure requires relatively large force to be applied to the tongue and the mandible while the user is trying to obtain a clear view of the glottis. Therefore, we integrated an independent rigid-body dynamics model with a virtual coupling scheme in parallel to the PBD model to account for collisions between the virtual tool and rigid objects, such as bones, and to prevent the virtual tool from penetrating soft tissues due to large forces.

3 SYSTEM OVERVIEW

Our VR-based immersive ETI simulation system includes a HTC® Vive™ Pro head-mounted display (HMD) with one hand controller, a Geomagic® Touch™ X haptic device (6 degree of freedom (DOF), 3 degree of force output) and a trakSTAR™ EM sensor (6 DOF) (Fig. 1). The HMD with combined resolution of 2880×1600 pixels allows the user to perform the procedure in the virtual environment from any viewpoint in a more natural way than in screen-based computer simulators. The hand controller is used to adjust various parameters in the VR simulator, such as head elevation, operation table angle and jaw opening, and to perform oral suction. The haptic device and the EM sensor allow bimanual interaction with the virtual laryngoscope and the ETT during the procedure. To further improve the sensation of grasping the laryngoscope and the ETT, 3D printed laryngoscope handle and ETT connector modeled on measurements of a Miller 1 laryngoscope and a 3.0 mm ETT were attached to the haptic device and the EM sensor respectively. The workspace of the haptic end effector spans a volume of approximately 160×120×120 mm³, which is sufficient to cover the volume of the motions for the ETI procedure. The motion was captured in 3D allowing for real-time and post-trial viewing, visualization from different angles (cross-sectional and video laryngoscopic views) (Fig. 1) and measurements on the virtual model during the procedure. The motion data were recorded throughout the entire procedure and streamed to a computer for post-trial assessment and statistical analysis.

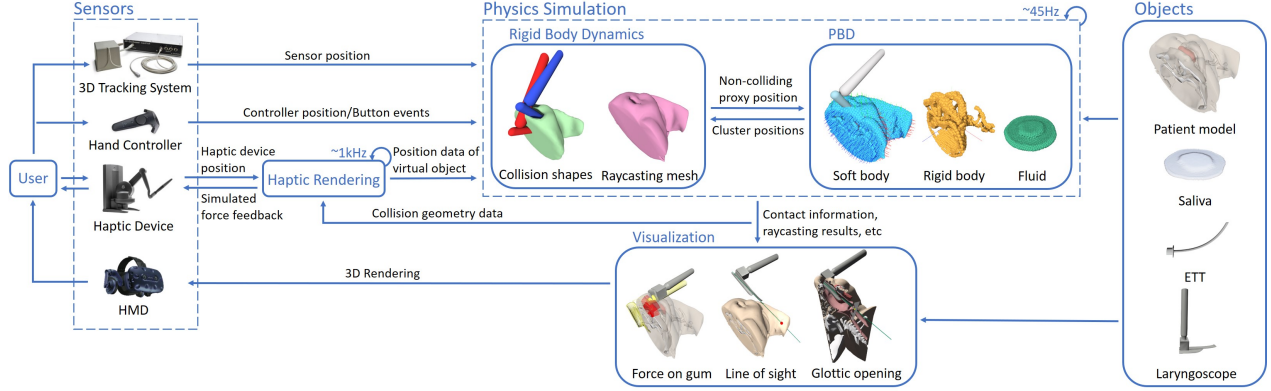


Figure 2: System architecture showing interaction flow.

An overview of the proposed architecture is provided in Fig. 2. It consists of a main simulation program, an object representation structure (object class) and an abstraction of I/O devices (sensor class). The main simulation program contains the simulation functions and processes the dynamics of objects (deformable or rigid-body dynamics) and their communication with each other. Each object is decomposed into various representations where each representation is more suited toward a particular task - modeling, collision detection and visualization. These representations are linked together so they can be updated coherently. In this way, objects in the PBD layer are able to communicate with objects in the rigid-body dynamics layer.

Our framework uses PBD to simulate the behavior of human body constituents, such as soft tissues, bones and fluids (e.g., blood, secretions), in a unified particle representation, which allows for seamless modeling of different substances [17]. In parallel, an independent rigid-body dynamics model was integrated to account for collisions between the virtual laryngoscope and bones and to prevent the virtual tool from penetrating soft tissues due to large interaction forces. In addition, it provides functionalities, such as contact callbacks, raycasting, etc. for developing real-time visualization. The details of the simulation algorithm will be addressed in the following sections.

3.1 System Setup and Calibration

The framework interfaces with many different interaction devices through the sensor class. A calibration procedure was performed by a technician before the experiment to register each sensor into the same coordinate system. We first calibrated the Vive™ system and set its coordinate system as the world space. We then registered the haptic device into the world space. Two sets of corresponding 3D points were collected by waving the haptic arm and the hand controller, with the haptic interface tip pointing at a known position on the hand controller. With the acquired 3D point correspondences, the optimal least square best-fit rigid transformation from the haptic space to the world space was found by the singular value decomposition algorithm [1]. Similarly, we registered the 3D tracking system space to the world space for the EM sensor. With the system fully calibrated (errors under 2 mm), both the 3D printed laryngoscope and ETT were registered to their virtual counterparts and users had no trouble locating the instruments while they were in the virtual environment.

3.2 Segmentation

Our virtual simulator was built on a model of CT scans of a real neonatal patient. The stack of CT images forms a 3D volume that contains the head of a neonate (Fig. 3). The mouth, jaws, tongue and airway are the anatomical regions that are directly involved in a neonatal ETI. For simplicity, we segmented the model into three

parts: body tissue (including mouth and airway), tongue and bone (including upper/lower jaws). We separated the tongue from the body tissue to allow for varying the size of the tongue or changing the tongue models to simulate different levels of difficulty. In addition, the parameterized model enables adjustments in many other features including head size, jaw opening and mouth secretions. We segmented the CT model in ITK-SNAP [36] and exported the resulting segmentations into surface meshes, which were further smoothed and simplified.

4 POSITION-BASED SIMULATION

Our system uses PBD to simulate hybrid scenarios with rigid, soft and fluid objects using a unified particle representation [17] [25]. The objects to be simulated are represented by a set of N particles and M constraints that describe the objects. Each particle has three attributes, namely position \mathbf{p}_i , velocity \mathbf{v}_i and mass m_i . Aside from these attributes, each particle has a phase identifier that controls how they behave and collide with other particles. Each object is represented by a group of particles that have the same phase, which acts as a collision filter used for collision detection against other groups of particles. Let \mathbf{p} be the concatenation $[\mathbf{p}_1^T, \dots, \mathbf{p}_N^T]^T$ and let each constraint function C_j , $j \in [1, \dots, M]$ take the concatenated vector \mathbf{p} as input while only using the subset of coordinates they are defined for. PBD solves a system of non-linear equality and inequality constraints such that $C_j(\mathbf{p}) \succ 0$, where the symbol \succ denotes either $=$ or \geq . Constraints are solved using the Gauss-Seidel method. For each iteration, constraints are solved sequentially through a linearization in the neighborhood of the current solution $C(\mathbf{p})$ using

$$C(\mathbf{p} + \Delta\mathbf{p}) \approx C(\mathbf{p}) + \nabla_{\mathbf{p}}C(\mathbf{p}) \cdot \Delta\mathbf{p} = 0. \quad (1)$$

The position displacement $\Delta\mathbf{p}$ is restricted to be in the direction of $\nabla_{\mathbf{p}}C$, which conserves the linear and angular momenta. This means that only one scalar λ - a Lagrange multiplier - has to be found such that the correction

$$\Delta\mathbf{p} = \lambda \nabla_{\mathbf{p}}C(\mathbf{p}) \quad (2)$$

solves Equation (1). This yields the following formula for $\Delta\mathbf{p}$:

$$\Delta\mathbf{p} = -\frac{C(\mathbf{p})}{|\nabla_{\mathbf{p}}C(\mathbf{p})|^2} \nabla_{\mathbf{p}}C(\mathbf{p}). \quad (3)$$

After each constraint has been solved, positions are updated. After a specified number of iterations, the change in velocity is determined by the total constraint displacement

$$\Delta\mathbf{v} = \Delta\mathbf{p}/\Delta t, \quad (4)$$

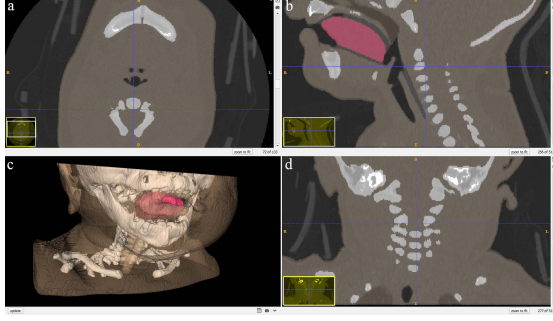


Figure 3: Segmentation results. Windows a, b and d display the image volume in the orthogonal axial, sagittal and coronal planes respectively. Window c displays the 3D view of the volume. The color coding highlights different areas of segmentation.

where Δt is the time step. Inequality constraints are handled trivially by first checking whether $C(\mathbf{p}) \geq 0$. If this is the case, the constraint is simply skipped.

In PBD, deformable objects can be simulated by adding geometrically motivated shape-matching constraints [22]. This method is based on finding the least square optimal rigid transformation in 3D between two sets of points with *a priori* known correspondence. The algorithm requires a set of particles with masses m_i and their respective initial positions \mathbf{p}_i^0 as input. At each time step, the original shape \mathbf{p}_i^0 is matched to the deformed shape \mathbf{p}_i . Then, the deformed points \mathbf{p}_i are forced towards the goal positions \mathbf{g}_i . Given two sets of points \mathbf{p}_i^0 and \mathbf{p}_i , the minimization problem is given by

$$\sum_i m_i (\mathbf{R}(\mathbf{p}_i^0 - \mathbf{t}_0) + \mathbf{t} - \mathbf{p}_i)^2, \quad (5)$$

where m_i are the masses of individual particles, \mathbf{R} is the rotation matrix, \mathbf{t} and \mathbf{t}_0 are the translation vectors given by the center of mass of the initial shape $\bar{\mathbf{p}}^0$ and the deformed shape $\bar{\mathbf{p}}$ respectively. Once the optimal rotation \mathbf{R} and translation vector \mathbf{t} are derived, the goal positions can be computed as

$$\mathbf{g}_i = \mathbf{R}(\mathbf{p}_i^0 - \bar{\mathbf{p}}^0) + \bar{\mathbf{p}}. \quad (6)$$

From the goal positions, an integration scheme can be defined

$$\mathbf{v}_i(t + \Delta t) = \mathbf{v}_i(t) + \alpha \frac{\mathbf{g}_i(t) - \mathbf{p}_i(t)}{\Delta t} + \frac{\Delta t \mathbf{f}_{ext}(t)}{m_i}, \quad (7)$$

$$\mathbf{p}_i(t + \Delta t) = \mathbf{p}_i(t) + \Delta t \mathbf{v}_i(t + \Delta t), \quad (8)$$

where $\alpha \in [0, 1]$ is a user defined stiffness parameter which defines how far the particles are pulled toward their goal positions.

The implementation of the algorithm described above allows only for small deformations from the initial shape. For larger deformations, e.g., to model soft tissue, the concept of cluster-based shape matching method can be integrated [8] [22] [30]. The idea is to divide the set of particles that comprise an object into multiple overlapping clusters (shape-matching constraints). Every cluster has its own position and rotation, which serve as “joint” for the object. Every particle is connected to one or more clusters with a weight between 0.0 and 1.0, which defines how much a cluster influences the transform of a particle. After performing shape matching for all clusters, we get multiple goal positions for each particle. The final goal position for a particle i is determined by blending the goal positions of the corresponding clusters \mathcal{C}_i that the particle belongs to:

$$\mathbf{g}_i = \frac{\sum_{j \in \mathcal{C}_i} \mathbf{R}_j(\mathbf{p}_i^0 - \bar{\mathbf{p}}_j^0) + \bar{\mathbf{p}}_j}{|\mathcal{C}_i|}. \quad (9)$$

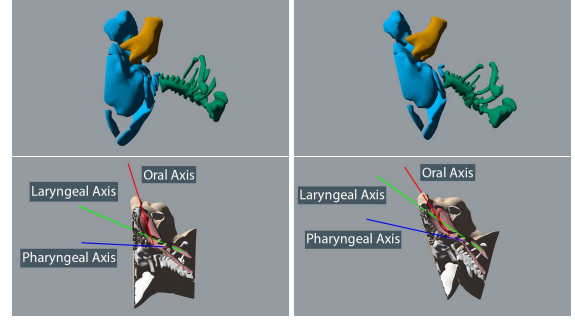


Figure 4: Skeletal structure of the model. (left) Original posture; (right) adjusted posture with head elevated and jaw opened. The oral, laryngeal and pharyngeal axes are superimposed on the model to help the user get the optimal head position before the procedure.

4.1 Rigid Body Simulation

We represented the skeletal structure in our simulation model as rigid bodies using particles and added a rigid shape-matching constraint [22] to each rigid body to maintain particle configurations. Particles were generated by first performing uniform voxelization of each bone mesh and placing particles at each occupied voxel interior to the mesh (Fig. 2). We then assigned all particles in each mesh the same phase identifier and added only one shape-matching constraint to the body so that all the particles are connected to one cluster with weight 1.0. In this way, the object is treated as a rigid body.

In order to simulate the motion of the patient’s head and mandible, an articulated skeletal structure was developed. We segmented the bones into 3 separate meshes as shown in Fig. 4. The joints of the skeleton were placed at the top of the neck and at the two ends of the mandible to simulate the movement of the cervical vertebrae and the mandible respectively. In order to keep the movements of the head and the mandible realistic, the joint at the neck allows for 30 degrees of vertical movement. The pair of joints at two ends of the mandible allows for 35 degrees of vertical movement. We set all the masses of the bone particles to infinity so that they are treated as static objects. We use the hand controller to adjust the head elevation and the jaw opening. Since there is only one cluster in each rigid body, we do not need any skinning for the corresponding mesh, all the mesh vertices are transformed accordingly by the rotation and the translation of that cluster.

4.2 Soft Tissue Deformation

We simulated soft tissues, such as the body tissue and the tongue, and the deformable ETT as soft bodies by using cluster-based shape matching constraints [22]. Particles were firstly generated using the same method as described previously for rigid bodies. We then generated multiple clusters for each soft body to allow larger deformations (Fig. 2). With different cluster spacing and stiffness, we can simulate different tissue properties. Each mesh of corresponding soft body is expressed in terms of local cluster positions through linear blend skinning [12]. As a result, the mesh will deform in accordance with the manipulated particles.

For this particular procedure, the ability to manipulate the epiglottis with the tip of the laryngoscope blade is critical because it determines if the user can get a clear view of the glottis, which affects the outcome of the overall procedure. However, clusters are uniformly generated and may not be dense enough to allow detailed deformations of small features, such as the epiglottis. Increasing the number of clusters or adaptively generating clusters according to geometric features could solve the problem but introducing a heavy computational overhead and may still not solve the problem perfectly. Therefore, our solution was to create an additional cluster

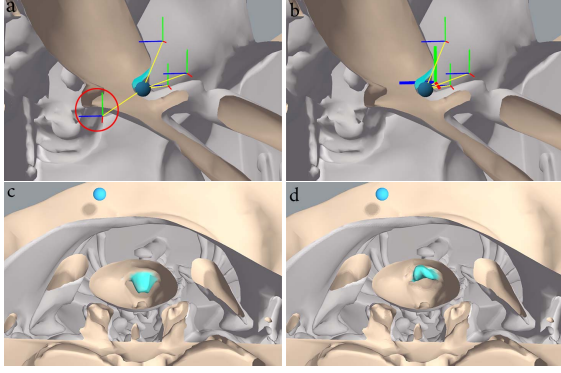


Figure 5: Cluster modification. (first row) Cross-sectional views of a particle on the epiglottis with its associated clusters before (a) and after (b) the cluster modification. (second row) Frontal views of a particle on the epiglottis dragged to the upper-left direction before (a) and after (b) the cluster modification.

(the local coordinate axes with thicker lines in Fig. 5(b)) at the center of the particles that belong to the epiglottis and assign all these particles to that cluster. At the same time, we removed any clusters from these particles that were incorrectly assigned. As shown in Fig. 5(a), some particles on the epiglottis were incorrectly connected to those clusters that were not geometrically close to them, which prevents the local deformation of the epiglottis (Fig. 5(c)). Lastly, we also removed incorrectly assigned clusters from these skinned mesh vertices on the epiglottis so that the mesh would be deformed correctly.

In order to make the body tissue move along with the skeletal structure realistically, we set the masses of the particles on the body tissue that are close to the bone particles to infinity. In this way, when the user adjusts the skeletal structure, the particles on the body tissue with infinite mass will be moved together. Since all the remaining particles on the body tissue are connected with the particles with infinite mass through shape-matching constraints, they will be deformed accordingly.

The tongue particles and clusters are generated in a similar way as the body tissue but with different cluster spacing and stiffness. We attached the tongue to the mouth by adding distance constraints between them. A slide bar panel is provided (Fig. 1) on the graphic user interface to allow the adjustment of the tongue size and other parameters that affect the intubation difficulty.

The ETT is also simulated as a soft body with adjustable stiffness. We set the masses of the particles on the ETT connector as infinity so that it is rigid, and its pose can be directly controlled by the EM sensor. The stiffness values of the body tissue, tongue and ETT were manually tuned during preliminary testing experiments, until suitable visual and tactile perceptions were achieved according to the feedback from an expert neonatologist.

4.3 Fluid Simulation

When performing ETI on real patients, intubators often encounter situations where patients have excessive secretions in their mouth, such as saliva, which prevent the intubators from getting a clear view of the glottis. Therefore, suction needs to be performed prior to the procedure. In order to mimic this real clinical situation, saliva was simulated as fluids in our system, which is based on position-based fluids [16]. This method uses position-based density constraints to achieve lower compression and better stability than traditional smoothed particle hydrodynamics (SPH) methods [20]. To enforce constant density, a constraint function

$$C_i(\mathbf{p}) = \rho_i / \rho_0 - 1 \leq 0 \quad (10)$$

was added to each fluid particle i . Each constraint C_i is a function of the particle's position and the positions of its neighbors. ρ_0 is the rest density and ρ_i is given by the standard SPH density estimator:

$$\rho_i = \sum_j m_j W(\mathbf{p}_i - \mathbf{p}_j, h), \quad (11)$$

where m_j are the masses of neighboring particles within the smoothing length radius of particle i , h is the smoothing length and W is the kernel function. Fluid particles were emitted from the locations of the salivary glands inside the mouth at a random speed during the procedure (Fig. 6(d)). The simulation of fluid suction was implemented by pulling the trigger on the hand controller. A high viscosity value was set to simulate viscous effect of the saliva.

5 COLLISION DETECTION

In the PBD simulation layer, the virtual model of the laryngoscope was approximated with simple collision shapes for fast collision detection against particles. We enclosed the handle and the blade of the laryngoscope within three capsule collision shapes (Fig. 6(b)). The haptic device provides the input position and orientation for the visual model of the laryngoscope and its collision shapes. Since the blade of the laryngoscope is approximated with two capsule shapes, the ETT cannot pass through the blade with no collision filter. Therefore, we only allow the blade capsule shapes to collide with other PBD objects by setting corresponding collision shape channels and the particle phase identifiers. We then created a signed distance field (SDF) collision shape that approximates the shape of the blade but thicker to achieve robust collision detection (Fig. 6(b)). We set this SDF collision shape to collide only with the ETT particles.

Another issue with the ETT is that it is composed of thin lines of particles, which are prone to penetrate other groups of particles. This makes it hard to insert the ETT into either the airway or the esophagus without penetration. Therefore, we created another SDF collision shape underneath the body by moving the body mesh inwards with a constant offset (Fig. 6(b)). This offset collision shape, on one hand, can prevent the ETT from penetrating the body tissue. On the other hand, it can prevent the tongue from penetrating the body tissue when the laryngoscope pushes the tongue against it. Moreover, when simulating saliva, this SDF collision shape can also prevent fluid particles from leaking through the body (Fig. 6(c) and Fig. 6(d)). We set this SDF collision shape to only collide with the ETT, the tongue and the saliva particles.

Since the laryngoscope under interaction is kinematic and free from physics in the virtual world, external forces from gravity or collisions will no longer have any effect on it because the position is set absolutely by the user. The held laryngoscope could still apply forces to dynamic objects that are free to move, but if it pushes a dynamic object against a static object (such as the body tissue attached to the bones), the held laryngoscope would easily penetrate the body tissue. Moreover, there is no interaction or collision between the held laryngoscope and static objects, such as the bones. Therefore, we integrated another rigid-body dynamics model [26] as an additional simulation layer in parallel to the PBD layer to account for the collisions for rigid objects.

In the rigid-body simulation layer, we created the same collision shape representation for the laryngoscope as was used in the PBD layer with three capsule shapes (Fig. 6(a)). The collision shape for the bones was approximated with a single mesh that is the same as the offset collision shape used in the PBD layer, which encloses all the bones (Fig. 6(a)). This offset collision shape can speed up the collision detection. It can also set a boundary for the amount of deformation that the laryngoscope could apply to the body tissue, preventing penetration. As in the PBD layer, the kinematic laryngoscope in the rigid-body simulation layer would have no interaction or collision with static objects. Therefore, we employed a virtual coupling scheme by creating a dynamic proxy laryngoscope and

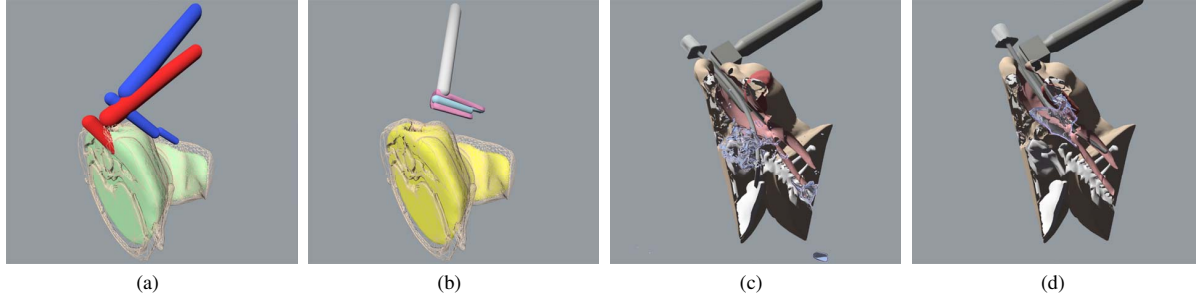


Figure 6: (a) and (b) are the collision shapes of the virtual model and the laryngoscope in the rigid-body dynamics layer and the PBD layer respectively; (c) and (d) are the simulation results before and after adding the SDF offset collision shape (yellow mesh in (b)). Without the offset collision shape, the ETT and the tongue easily penetrate the body tissue and the fluids are leaked through the body tissue.

constraining it to the kinematic laryngoscope (blue and red capsule shapes in Fig. 6(a)). While the kinematic laryngoscope could penetrate a collision shape, the proxy laryngoscope will respond to collisions and remain on the outside of the volume of the shape.

Both the offset body collision shapes in the PBD layer and the rigid-body dynamics layer are static collision shapes and need to be updated each time the user adjusts the position of the head, the table or the mandible. In each simulation cycle, the rigid-body dynamics layer fetches the cluster positions from the PBD layer to update its collision shapes through skinning. Conversely, the PBD layer receives the last non-colliding position of the proxy laryngoscope from the rigid-body dynamics layer to update the poses of its collision shapes of the laryngoscope.

6 HAPTIC FEEDBACK

The simulated force applied to the haptic device must be updated at a high rate of about 1kHz to maintain a realistic haptic feedback. However, the computational process of the collision detection, deformable models and the complex physical simulation are so time consuming that the required update rate of haptic force could not be guaranteed. Therefore, we implemented a multi-thread haptic rendering process to separate the haptic thread from the physical thread. In our implementation, we used two different approaches for computing the force response of the interaction of the laryngoscope with rigid bodies and with soft tissues.

To calculate the force feedback of rigid-body contacts, we first transformed the current position of the haptic interface and the non-colliding position of the proxy laryngoscope to the workspace of the haptic interface. Then, the force was calculated by simulating a virtual spring-damper between the kinematic and the proxy laryngoscope positions. The farther they are separated, the longer the spring is and hence greater resistance the user will feel, which impedes the motion of the haptic interface from further penetrating the object in contact.

For the force feedback during the interaction with soft tissues, collision tests between the proxy laryngoscope and the particles were computed in parallel in the haptic thread. We calculated the force as the average of all vectors pointing from the current positions of the particles (in contact with the proxy laryngoscope) to their rest positions (Fig. 7), which were backed up at the initialization of the simulation or reset after each time the user adjusted the position of the head, the table or the mandible. We calculated an average vector for each type of tissue that was in contact with the proxy laryngoscope and multiplied each vector by a constant factor μ (stiffness of each tissue type). We finally averaged all those vectors from each type of tissue to generate the force feedback from soft tissues. The summation of the forces due to interactions with rigid bodies and soft tissues was sent to the haptic device for force rendering.

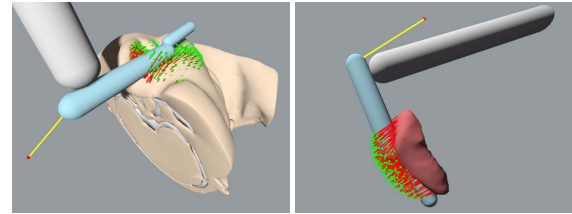


Figure 7: Calculation of soft tissue force feedback. The green points are the rest poses of the particles that are in contact with the laryngoscope. The red lines are the displacements of particles. The yellow line on the laryngoscope shows the resulting averaged displacement.

7 VISUALIZATION

With our manikin-free VR system, we can visualize an even larger set of performance parameters in relation to the internal geometric change of the virtual model during the entire procedure. Our full suite of enhanced visualization tools not only provide trainees with real-time feedback throughout the entire procedure, but also provide instructors with a clear understanding of what is happening during each step of an ETI, which is impossible in a manikin-based simulator. From the raw motion sequences, the simulation system extracted 12 primary performance parameters (Table 2). These parameters were chosen *a priori* based on the qualities that our expert instructor deemed as important features. We chose a subset of these parameters that are interpretable for direct visualization. The rest of the parameters are used only for statistical analysis. Based on the contact information and raycasting results returned from the rigid-body dynamics simulation layer, we calculated the force applied to the upper gums, laser dot of sight line showing the anatomical structures and the percentage of glottic opening that is visible to the subject, etc. (Fig. 2). All these parameters were rendered on the final visual models to guide the trainees during the procedure.

8 VALIDATION STUDY

8.1 Study Design

To quantify the relative realism of the VR simulator compared to the manikin-based simulator, we conducted an experimental study using a modified backward transfer or concurrent validation study [32]. The study was approved by the Children's National Health Systems' institutional review board. A group of experts (attending neonatologists) performed ETI on both the manikin-based augmented reality (AR) simulation system and the VR simulation system (Fig. 8). The AR system includes a standard full-term Laerdal® task trainer manikin, a laryngoscope with a Miller 1 blade and a 3.0 mm ETT,

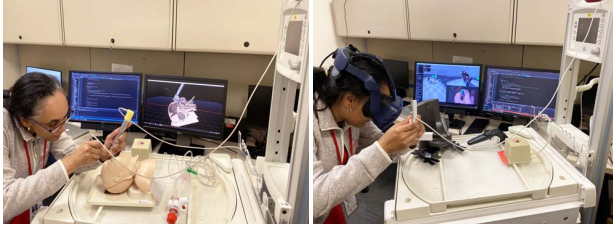


Figure 8: AR and VR setup for the validation study.

which were registered to their virtual CT scanned counterparts. The motion of the laryngoscope and the manikin were captured by trakSTAR™ EM sensors.

Four conditions were tested for each subject using a cross-over design: (1) using the AR system without enhanced visualization; (2) using the VR simulator without enhanced visualization; (3) using the VR simulator with increased level of difficulty (without enhanced visualization) and (4) using the VR simulator with enhanced visualization. In condition (2), subjects intubated a virtual patient that had the same size as the manikin in the AR system with a virtual Miller 1 blade and a virtual 3.0 mm ETT. In condition (3), the virtual patient was configured to a smaller premature infant size with relatively larger tongue and smaller jaw opening. The saliva simulation was turned on with specular light simulating glossy mouth. A virtual Miller 0 blade and a virtual 2.5 mm ETT were used. In condition (4), the virtual patient had the same configurations as the one in condition (2) but with full suite of enhanced visualization tools. Before using the AR and the VR simulators, the subjects were provided instructions on their use and given a chance to perform one successful intubation on each system. The order of using the AR or the VR system (condition (1) and condition (2)) was counterbalanced, and subjects were randomly assigned to each simulator. After that, each subject performed condition (3) and (4) respectively in the same order. During each intubation attempt, motions of the laryngoscope and the ETT were tracked and recorded.

8.2 Questionnaire & Measures

A questionnaire with 17 questions was administered immediately following the completion of certain conditions (Table 1). The questions were grouped into realism of anatomy and soft tissue, motion consistency of tools, difficulty of level change and acceptance of visualization. Lastly, each subject rated their overall recommendation for the VR simulator. Each question was scored on a 5-point Likert scale, where 1 stands for “very poor” and 5 stands for “very good” (For Q10, 1 = “much easier”, 5 = “much harder” and for Q17, 1 = “definitely not recommend”, 5 = “definitely recommend”). Subjective feedback and demographic information were collected at the end of the study.

After the trials, a team of 3 instructors (not including the participants themselves) viewed the 3D playback of motions and rated the performances under the 4 conditions using the enhanced visualization tools for both systems. Performance ratings consisted of a single score on a 5-point scale. Before rating the performances, the team engaged in a calibration exercise to maximize inter-rater reliability. The final ratings across instructors were averaged before analysis.

In addition, the computer systems extracted 8 primary performance parameters from the AR simulator and additional 4 more parameters from the VR simulator (Table 2). Among those parameters, the pitch/yaw related parameters were extracted from the angular displacements of the blade in the pitch/yaw directions during the procedure. In particular, pitch/yaw peaks are those peaks on corresponding angular curves that have a prominence of at least

Table 1: Results of the questionnaire.

Condition	Question	Mean (SD)	P-value
After (1) and (2)	1. Realism of Manikin anatomy	3.8 (0.83)	0.011
	2. Realism of VR anatomy	4.6 (0.53)	
	3. Realism of Manikin soft tissue	3.0 (1.00)	< 0.001
	4. Realism of VR soft tissue	4.6 (0.53)	
	5. Feel of Manikin	3.2 (0.97)	0.667
	6. Feel of VR patient	3.4 (1.13)	
	7. Motion consistency of scope	4.0 (1.32)	
	8. Motion consistency of ETT	3.2 (1.30)	
After (3)	9. Realism of saliva	3.7 (0.71)	
	10. Difficulty of level change	4.2 (0.97)	
	11. Helpfulness of three axes	4.4 (0.73)	
After (4)	12. Helpfulness of force indicator on upper gum	4.4 (0.53)	
	13. Helpfulness of laser dot	4.6 (0.53)	
	14. Helpfulness of percentage of glottic opening	4.1 (0.93)	
	15. Helpfulness of timer	4.2 (0.83)	
	16. Acceptance of overall visualization	4.4 (0.73)	
Overall	17. Recommendation of VR	4.9 (0.33)	

2.5-3.5 3.5-4.5 ≥ 4.5

5 degrees, which reflects the number of repositions of the blade. Pitch/yaw rocking were evaluated based on the maximum residual between the corresponding angular curves and their denoised curves by using wavelet transform, which quantifies the displacement of the largest reposition of the blade. Data were analyzed using software developed in-house [34] and Matlab®. To compare participants’ ratings, performance scores and parameters between manikin and VR simulators, different levels of difficulty and with/without visualization, we performed bootstrap paired mean tests. A P -value ≤ 0.05 implies a statistically significant difference between two conditions.

8.3 Results

In total, 15 subjects participated in the study, with an age range of 30-61 years. The subjects have an average of 14 years of work experience in neonatal intubation. The results of the questionnaire are summarized in Table 1. Subjects’ performance scores and parameters are presented in Fig. 9 and Table 2.

8.3.1 Comparison between Manikin and VR

With respect to the realism of the anatomy (Q1 vs. Q2) and the soft tissue (Q3 vs. Q4) compared to live patients, subjects have rated significantly in favor of the VR simulator ($P = 0.011$ and $P < 0.001$) (Table 1). In addition, though not significant, the feelings of manikin and VR patient (Q5 vs. Q6) compared to live patients are on average better for the VR simulator ($P = 0.667$). For the motion consistency of virtual tools (Q7 and Q8) in the VR simulator, subjects gave an average score of 4.0 for the laryngoscope and an average score of 3.2 for the ETT.

The relatively lower ratings on questions from Q6 to Q8 are associated with the hardware limitations of the haptic device and the EM sensor. 56% of the subjects pointed out that the haptic force was not strong enough to stop them from moving forward when the virtual laryngoscope had a collision. Moreover, 33% of the subjects noticed that there was no force resistance from the upper gums when they were rotating the blade to get a view of the glottis. These motion inconsistencies can probably be explained by the fact that the haptic device lacks torque output from rotational movements and has a maximum force output. Therefore, torque output from 6 DOF force feedback devices with stronger maximum forces would solve the problem and could be integrated in the future. For Q8,

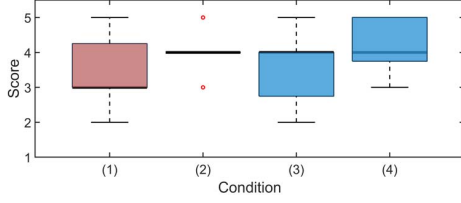


Figure 9: Results of performance scores rated by experts for 4 conditions.

44% of subjects noticed that they could not feel the force resistance from insertion of the ETT into the mouth, which is due to the fact that the EM sensor does not offer force feedback. Another haptic device or other devices with force feedback would solve the problem. Also, 78% of the subject said that the virtual ETT was too floppy compared to real ETTs and hard to control its movement. This is a limitation of the physics simulation, which is a trade-off between precision and robustness.

The average score of subjects' performances rated by instructors on VR for condition (2) is higher than that on the manikin (4.0 vs. 3.4), even though the difference did not reach statistical significance ($P = 0.105$) (Fig. 9). With respect to the subjects' performance parameters in those two conditions, the average force on gum and pitch rocking are both significantly lower on VR than those on manikin ($P = 0.028$ and $P < 0.001$) (Table 2), which indicate subjects performed better ETI on the VR patient than on the manikin. There is no significant difference on the rest of the parameters except the time, which is significantly longer on VR than on manikin ($P < 0.001$). This can probably be explained by the fact that all the subjects had experience with manikin-based simulators, but only one of them had experience with VR simulators and none with video games.

8.3.2 Comparison between Levels of Difficulty

The difficulty of condition (3) (Q10) has been rated much harder compared to condition (2), with an average score of 4.2 (Table 1). The result indicates that the VR simulator has the ability to simulate different levels of difficulty, which is one important advantage over manikin-based simulators. This is essential in developing expertise and preventing trainees from learning the skills by memory. The realism of saliva received an average score of 3.7. Even though not strongly positive, all the subjects stated that the simulation of saliva was realistic enough to distract them from getting a clear view of the glottis. 44% of the subjects suggested that the saliva should have a foamier appearance.

In addition, though not statistically significant, the average score in condition (3) is lower than that in condition (2) (3.6 vs. 4.0, $P = 0.215$) (Fig. 9). With respect to the performance parameters, there are significant increases in pitch peaks and rocking in condition (3) compared to condition (2) ($P = 0.022$ and $P = 0.024$) (Table 2), which indicate that increasing the difficulty level caused more repetitions of the blade with a larger maximum displacement. Moreover, the subjects had more attempts ($P = 0.042$) and spent longer time ($P = 0.008$) with increased level of difficulty. The maximum and mean depth in condition (3) are both significantly smaller than that in condition (2) ($P < 0.001$ and $P < 0.001$), which is because the virtual model in condition (3) is a premature infant.

8.3.3 Evaluation of Enhanced Visualization

All the questions regarding the enhanced visualization (Q11 to Q16) received average scores above 4.0, which indicate that our visualization tools are helpful in guiding trainees during the procedure. In particular, the visualization of the laser dot of sight line received an average score of 4.6, which indicates that the identification of the

Table 2: Results of performance parameters for 4 conditions. Mean (SD) values are presented for each parameter. For force, depth, glottic opening and ETT velocity, the maximum (first row) and mean (second row) values were both extracted from the corresponding time sequences of each subject.

	(1)	(2)	(3)	(4)
Force on gum	5.3 (2.98)	4.6 (2.45)	5.0 (2.31)	3.1 (1.36)
	3.2 (1.45)	1.8 (1.41)	1.7 (1.09)	1.5 (1.06)
Depth	7.3 (0.88)	7.3 (0.55)	5.4 (0.64)	7.3 (0.72)
	5.5 (0.67)	5.8 (0.66)	4.0 (0.74)	5.4 (0.50)
Pitch peaks	3.9 (2.32)	3.4 (1.94)	8.2 (2.83)	2.3 (1.00)
Yaw peaks	4.2 (3.23)	4.4 (2.13)	9.4 (3.01)	2.7 (0.87)
Pitch rocking	6.7 (1.88)	5.2 (0.67)	6.8 (1.56)	5.4 (0.58)
Yaw rocking	5.2 (1.54)	5.5 (1.00)	5.5 (0.67)	4.2 (0.16)
Attempts	1.0 (0.00)	1.0 (0.00)	1.7 (0.52)	1.0 (0.00)
Time	17.3 (5.18)	28.6 (6.78)	59.7 (28.19)	20.3 (6.83)
Percentage of glottic opening		69.7 (14.56)	54.1 (32.08)	81.5 (23.87)
		62.3 (13.21)	42.2 (38.75)	78.6 (25.30)
ETT Velocity		18.5 (5.72)	32.6 (28.16)	19.9 (7.21)
		6.1 (1.51)	5.8 (2.68)	8.1 (2.84)
Head angle		18.0 (7.57)	17.7 (8.84)	21.2 (4.23)
Blade slips		0.3 (0.50)	0.8 (0.76)	0.1 (0.33)

glottis is one of the most critical factors in performing a successful intubation.

Subjects' scores are on average higher in condition (4) compared to their scores in condition (2) (4.2 vs. 4.0, $P = 0.517$) (Fig. 9). By comparing the performance parameters between these two conditions (Table 2), the maximum force on gum, the yaw peaks/rocking and the time are all significant lower in condition (4) ($P = 0.014$, $P < 0.001$, $P < 0.001$ and $P = 0.002$). Though not significant, both the maximum and the mean percentage of glottic opening are on average higher in condition (4) with enhanced visualization than in condition (2) ($P = 0.192$ and $P = 0.091$). On average the head angles are also larger in condition (4) than those in condition (2) (21.2° vs. 17.7°, $P = 0.124$), which are closer to the optimal angle for intubation of the virtual patient (26°).

9 CONCLUSION

In this paper, we have presented, to the best of our knowledge, the first practical and efficient simulation framework that offers a completely new ETI training platform with realistic and configurable immersive virtual environments. The PBD approach has proven its efficiency and simplicity in simulating complex scenarios with rigid bones, soft tissues and fluids in a unified particle representation at interactive rates. While the results of this paper contribute primarily to neonatal ETI procedure, the interaction approach and simulation could be easily adapted to other multi-modal surgical simulation scenarios that involve interactions between surgical tools and rigid/deformable anatomical structures in virtual environments. Results from the validation study indicate the anatomy and soft tissue of our VR simulator are more realistic than the manikin simulator. Most importantly, our VR simulator is capable of simulating varying levels of difficulty, capturing a whole set of performance parameters and visualizing the events occurring within the patient model, making the approach a promising platform for training ETI.

ACKNOWLEDGMENTS

Research reported in this publication was supported by the Eunice Kennedy Shriver National Institute of Child Health & Human Development of the National Institutes of Health under Award Number R01HD091179. The content is solely the responsibility of the authors and does not necessarily represent the official views of the National Institutes of Health.

REFERENCES

- [1] K. S. Arun, T. S. Huang, and S. D. Blostein. Least-squares fitting of two 3-d point sets. *IEEE Transactions on pattern analysis and machine intelligence*, (5):698–700, 1987.
- [2] J. Bender, K. Erleben, and J. Trinkle. Interactive simulation of rigid body dynamics in computer graphics. In *Computer Graphics Forum*, vol. 33, pp. 246–270. Wiley Online Library, 2014.
- [3] J. Bercic, M. Pocajt, and J. Drzecnik. The influence of tracheal vascularization on the optimum location, shape and size of the tracheostomy in prolonged intubation. *Resuscitation*, 6(2):131–143, 1978.
- [4] I. Berndt, R. Torchelsen, and A. Maciel. Efficient surgical cutting with position-based dynamics. *IEEE computer graphics and applications*, 37(3):24–31, 2017.
- [5] M. Camara, E. Mayer, A. Darzi, and P. Pratt. Soft tissue deformation for surgical simulation: a position-based dynamics approach. *International journal of computer assisted radiology and surgery*, 11(6):919–928, 2016.
- [6] S. D. DeMeo, L. Katakam, R. N. Goldberg, and D. Tanaka. Predicting neonatal intubation competency in trainees. *Pediatrics*, 135(5):e1229–e1236, 2015.
- [7] D. Demirel, Y. Alexander, T. Halic, G. Sankaranarayanan, A. Ryason, D. Spindler, K. L. Butler, C. Caroline, E. Petrusa, M. Molina, et al. Virtual airway skills trainer (vast) simulator. *Studies in health technology and informatics*, 220:91, 2016.
- [8] R. Diziol, J. Bender, and D. Bayer. Robust real-time deformation of incompressible surface meshes. In *Proceedings of the 2011 ACM SIGGRAPH/eurographics symposium on computer animation*, pp. 237–246. ACM, 2011.
- [9] E. E. Foglia, A. Ades, N. Napolitano, J. Leffelman, V. Nadkarni, and A. Nishisaki. Factors associated with adverse events during tracheal intubation in the nicu. *Neonatology*, 108(1):23–29, 2015.
- [10] L. D. Hatch, P. H. Grubb, A. S. Lea, W. F. Walsh, M. H. Markham, G. M. Whitney, J. C. Slaughter, A. R. Stark, and E. W. Ely. Endotracheal intubation in neonates: a prospective study of adverse safety events in 162 infants. *The Journal of pediatrics*, 168:62–66, 2016.
- [11] S. A. Heredia-Pérez, K. Harada, M. A. Padilla-Castañeda, M. Marques-Marinho, J. A. Márquez-Flores, and M. Mitsuishi. Virtual reality simulation of robotic transsphenoidal brain tumor resection: Evaluating dynamic motion scaling in a master-slave system. *The International Journal of Medical Robotics and Computer Assisted Surgery*, 15(1):e1953, 2019.
- [12] L. Kavan. Part i: direct skinning methods and deformation primitives. In *ACM SIGGRAPH*, vol. 2014, pp. 1–11, 2014.
- [13] C. Konrad, G. Schupfer, M. Wietlisbach, and H. Gerber. Learning manual skills in anesthesiology: is there a recommended number of cases for anesthetic procedures? *Anesthesia & Analgesia*, 86(3):635–639, 1998.
- [14] B. Kubiak, N. Pietroni, F. Ganovelli, and M. Fratarcangeli. A robust method for real-time thread simulation. In *Proceedings of the 2007 ACM symposium on Virtual reality software and technology*, pp. 85–88. ACM, 2007.
- [15] J. Lubin and R. Carter. The feasibility of daily mannequin practice to improve intubation success. *Air medical journal*, 28(4):195–197, 2009.
- [16] M. Macklin and M. Müller. Position based fluids. *ACM Transactions on Graphics (TOG)*, 32(4):104, 2013.
- [17] M. Macklin, M. Müller, N. Chentanez, and T.-Y. Kim. Unified particle physics for real-time applications. *ACM Transactions on Graphics (TOG)*, 33(4):153, 2014.
- [18] J. Mayrose, T. Kesavadas, K. Chugh, D. Joshi, and D. G. Ellis. Utilization of virtual reality for endotracheal intubation training. *Resuscitation*, 59(1):133–138, 2003.
- [19] J. Mayrose and J. W. Myers. Endotracheal intubation: application of virtual reality to emergency medical services education. *Simulation in Healthcare*, 2(4):231–234, 2007.
- [20] J. J. Monaghan. Smoothed particle hydrodynamics. *Annual review of astronomy and astrophysics*, 30(1):543–574, 1992.
- [21] M. Müller, B. Heidelberger, M. Hennix, and J. Ratcliff. Position based dynamics. *Journal of Visual Communication and Image Representation*, 18(2):109–118, 2007.
- [22] M. Müller, B. Heidelberger, M. Teschner, and M. Gross. Meshless deformations based on shape matching. *ACM transactions on graphics (TOG)*, 24(3):471–478, 2005.
- [23] A. Nealen, M. Müller, R. Keiser, E. Boxerman, and M. Carlson. Physically based deformable models in computer graphics. In *Computer graphics forum*, vol. 25, pp. 809–836. Wiley Online Library, 2006.
- [24] A. Nishisaki, A. J. Donoghue, S. Colborn, C. Watson, A. Meyer, C. A. Brown, M. A. Helfaer, R. M. Walls, and V. M. Nadkarni. Effect of just-in-time simulation training on tracheal intubation procedure safety in the pediatric intensive care unit. *Anesthesiology: The Journal of the American Society of Anesthesiologists*, 113(1):214–223, 2010.
- [25] NVIDIA Gameworks. Flex from <https://developer.nvidia.com/flex>. 2018.
- [26] NVIDIA Gameworks. Physx from <https://developer.nvidia.com/gameworks-physx-overview>. 2018.
- [27] J. L. Plummer and H. Owen. Learning endotracheal intubation in a clinical skills learning center: a quantitative study. *Anesthesia & Analgesia*, 93(3):656–662, 2001.
- [28] K. Qian, J. Bai, X. Yang, J. Pan, and J. Zhang. Virtual reality based laparoscopic surgery simulation. In *Proceedings of the 21st ACM Symposium on Virtual Reality Software and Technology*, pp. 69–78. ACM, 2015.
- [29] P. Rajeswaran, N.-T. Hung, T. Kesavadas, J. Vozenilek, and P. Kumar. Airwayvr: Learning endotracheal intubation in virtual reality. In *2018 IEEE Conference on Virtual Reality and 3D User Interfaces (VR)*, pp. 669–670. IEEE, 2018.
- [30] A. R. Rivers and D. L. James. Fastlsm: fast lattice shape matching for robust real-time deformation. In *ACM Transactions on Graphics (TOG)*, vol. 26, p. 82. ACM, 2007.
- [31] R. C. Sanders, J. S. Giuliano, J. E. Sullivan, C. A. Brown, R. M. Walls, V. Nadkarni, A. Nishisaki, N. E. A. R. for Children Investigators, P. A. L. Injury, S. I. Network, et al. Level of trainee and tracheal intubation outcomes. *Pediatrics*, 131(3):e821–e828, 2013.
- [32] R. E. Sedlack, T. H. Baron, S. M. Downing, and A. J. Schwartz. Validation of a colonoscopy simulation model for skills assessment. *The American journal of gastroenterology*, 102(1):64, 2007.
- [33] R. D. Stewart, P. M. Paris, G. H. Pelton, and D. Garretson. Effect of varied training techniques on field endotracheal intubation success rates. *Annals of emergency medicine*, 13(11):1032–1036, 1984.
- [34] X. Xiao, W. Li, C. Clawson, D. Karvani, P. Sondag, and J. K. Hahn. Evaluation of performance, acceptance, and compliance of an auto-injector in healthy and rheumatoid arthritic subjects measured by a motion capture system. *Patient preference and adherence*, 12:515, 2018.
- [35] J. Yang, Y. Kim, H. Chung, J. Cho, H. Lee, G. Kang, E. Kim, T. Lim, and Y. S. Cho. Comparison of four manikins and fresh frozen cadaver models for direct laryngoscopic orotracheal intubation training. *Emergency Medicine Journal*, 27(1):13–16, 2010.
- [36] P. A. Yushkevich, J. Piven, H. Cody Hazlett, R. Gimpel Smith, S. Ho, J. C. Gee, and G. Gerig. User-guided 3D active contour segmentation of anatomical structures: Significantly improved efficiency and reliability. *Neuroimage*, 31(3):1116–1128, 2006.